Ocean Modelling 102 (2016) 82–98

Contents lists available at ScienceDirect

Ocean Modelling

journal homepage: www.elsevier.com/locate/ocemod

Spatial heterogeneity of ocean surface boundary conditions under sea ice

Antoine Barthélemy*, Thierry Fichefet, Hugues Goosse

Georges Lemaître Centre for Earth and Climate Research (TECLIM), Earth and Life Institute, Université catholique de Louvain, Louvain-la-Neuve, Belgium

ARTICLE INFO

Article history:
Received 17 November 2015
Revised 10 March 2016
Accepted 15 May 2016
Available online 16 May 2016

Keywords:
Model
Ocean surface boundary conditions
Ice thickness distribution
Arctic
Antarctic

ABSTRACT

The high heterogeneity of sea ice properties implies that its effects on the ocean are spatially variable at horizontal scales as small as a few meters. Previous studies have shown that taking this variability into account in models could be required to simulate adequately mixed layer processes and the upper ocean temperature and salinity structures. Although many advanced sea ice models include a subgrid-scale ice thickness distribution, potentially providing heterogeneous surface boundary conditions, the information is lost in the coupling with a unique ocean grid cell underneath. The present paper provides a thorough examination of boundary conditions at the ocean surface in the NEMO-LIM model, which can be used as a guideline for studies implementing subgrid-scale ocean vertical mixing schemes. Freshwater, salt, solar heat and non-solar heat fluxes are examined, as well as the norm of the surface stress. All of the thermohaline fluxes vary considerably between the open water and ice fractions of grid cells. To a lesser extent, this is also the case for the surface stress. Moreover, the salt fluxes in both hemispheres and the solar heat fluxes in the Arctic show a dependence on the ice thickness category, with more intense fluxes for thinner ice, which promotes further subgrid-scale heterogeneity. Our analysis also points out biases in the simulated open water fraction and in the ice thickness distribution, which should be investigated in more details in order to ensure that the latter is used to the best advantage.

1. Introduction

The presence of sea ice at the polar oceans surface has numerous impacts on their upper layer physics and biogeochemistry. Its high albedo compared to seawater strongly reduces the amount of absorbed solar radiation, giving rise to the well-known positive ice-albedo feedback (Curry et al., 1995). It constitutes an efficient barrier for mass exchanges between the atmosphere and the sea surface, inhibiting evaporation and preventing at least a fraction of precipitation from entering the ocean at the time when it falls. Owing to its low thermal conductivity (Pringle et al., 2007), sea ice dampens the oceanic heat losses to the atmosphere in winter. Because its salinity is lower than that of the sea surface, and because it is transported by winds and currents, its formation and melt are associated with buoyancy fluxes that influence the upper ocean stratification, convective processes and eventually the global thermohaline circulation (e.g., Goosse and Fichefet, 1999). A compact sea ice cover prevents the formation of waves and direct wind-generated turbulence in the water column, but its relative motion with respect to the water is a source of stress at the ocean surface. From a biogeochemical point of view, sea ice modulates the gas exchanges at the atmosphere-ice-ocean interface, provides a support for microbiological activity and chemistry, and acts to concentrate, transport or release nutrients and substances like inorganic carbon (Vancoppenolle et al., 2013).

The sea ice cover is a fundamentally heterogeneous medium. During summer, large open water areas can exist between the melting floes. A few percent of the sea surface remain free of ice even at the core of the winter season, in the form either of linear openings caused by divergence of the pack, known as leads, or of polynyas created by strong winds or high oceanic heat supply. The ice itself is a mixture of components ranging from thin new ice formed in open water areas to ridges several meters thick resulting from deformation inside the pack (Thorndike et al., 1975). While the most substantial differences in surface conditions occur between ice-covered and ice-free areas, several of the processes listed above also depend on the sea ice type, thickness and surface state. As these vary significantly on small horizontal scales, so do their effects on the underlying ocean and the atmosphere above.

It has long been recognized important to represent the subgrid-scale heterogeneity of ice thickness in order to accurately simulate the sea ice evolution (Thorndike et al., 1975; Hibler, 1980). As a

* Corresponding author. Georges Lemaître Centre for Earth and Climate Research, place Louis Pasteur 3, box L4.03.08, 1348 Louvain-la-Neuve, Belgium.
E-mail addresses: antoine.barthelemy@uclouvain.be (A. Barthélemy), thierry.fichefet@uclouvain.be (T. Fichefet), hugues.goosse@uclouvain.be (H. Goosse).

http://dx.doi.org/10.1016/j.ocemod.2016.05.003
1463-5003/

consequence, ice thickness distributions are included in most advanced models nowadays, among which CICE (Los Alamos Sea Ice Model, Hunke et al., 2015) and PIOMAS (Pan-Arctic Ice-Ocean Modeling and Assimilation System, Zhang and Rothrock, 2003). It allows them to compute the open water fraction and the concentration of ice of various thicknesses based on thermodynamic and dynamic processes. The implementation details and the impacts on model results are likewise intensively studied (e.g., Massonnet et al., 2011; Komuro and Suzuki, 2013; Castro-Morales et al., 2014; Hunke, 2014). However, the spatial heterogeneity in ocean surface boundary conditions implied by this variability in ice properties has been so far overlooked. This is explained by the fact that the various ice thickness categories have to exchange information with a unique ocean grid cell underneath, which requires the fluxes to be aggregated into single values.

Previous studies have shown that taking the surface conditions heterogeneity into account is necessary in order to adequately simulate the ocean physics below sea ice. By comparing vertical mixing parameterizations commonly used in coarse resolution large-scale models with large eddy simulations, (Losch et al., 2006) have demonstrated that neglecting the heterogeneous nature of buoyancy fluxes associated with a partial ice cover leads to biases in the mixed layer depth and the upper ocean density structure. Brine rejection parameterizations have for instance been developed to represent the impacts of intense convective mixing in winter leads (e.g., Duffy and Caldeira, 1997; Nguyen et al., 2009; Barthélemy et al., 2015). Further studies have implemented explicit separate vertical mixing computations in fractions of individual grid cells corresponding to ice and to open water (Holland, 2003; Jin et al., 2015).

Nevertheless, a detailed description of the heterogeneous ocean surface boundary conditions under sea ice is still missing, to our knowledge. The objective of the present paper is therefore to fill in this gap. In addition to leading to a better understanding of the spatial distribution of sea ice-ocean interactions, this will be of great interest to help interpreting the results of the above-mentioned studies. Under-ice observations are still far too sparse to allow examining under-ice fluxes at large scale and in all seasons. Our study will hence make use of the global ocean-sea ice model NEMO-LIM, whose ice component includes a state-of-the-art ice thickness distribution and in which the subgrid-scale heterogeneity of all fluxes and of the stress provided at the ocean surface will be thoroughly investigated.

This paper is organized as follows. The NEMO-LIM model setup is described in Section 2, with a particular emphasis on the ocean surface boundary condition aspects. The modeled mean sea ice state and ice thickness distribution are documented in Section 3, because they constitute the background for the simulation of heterogeneous boundary conditions. The latter are presented and discussed in Section 4. A summary of our findings is finally given in Section 5.

2. Model setup

2.1. Ocean-sea ice model NEMO-LIM

The ocean component of NEMO (Nucleus for European Modelling of the Ocean) is a finite difference, hydrostatic, free surface, primitive equation model fully described in Madec (2008). The ocean model's version 3.5 is coupled to the latest revision of the dynamic-thermodynamic sea ice model LIM (Louvain-la-Neuve sea Ice Model), known as LIM3.6 (Vancoppenolle et al., 2009; Rousset et al., 2015). LIM includes an ice thickness distribution (ITD), which allows to represent the subgrid-scale heterogeneity of ice thickness, enthalpy and salinity. A C-grid formulation of the elastic-viscous-plastic rheology is utilized for ice dynamics (Bouillon et al., 2013). The model configuration is very close to the one used in Barthélemy et al. (2015). Three noticeable differences are listed hereafter, along with details about the ocean surface boundary conditions (SBCs) and the experimental design.

First, compared to Barthélemy et al. (2015), we use a slightly updated version of LIM, in which several minor heat conservation leaks have been fixed (Rousset et al., 2015).

Second, the background diffusivity in the so-called TKE vertical mixing scheme (for turbulent kinetic energy, Blanke and Delecluse, 1993; Madec, 2008) has been lowered in the polar regions, following studies showing that it improves Arctic Ocean simulations (Zhang and Steele, 2007; Nguyen et al., 2009; Komuro, 2014). In practice, a tenfold reduction of the background vertical diffusivity poleward of 60° N and of 60° S is implemented, whereas the reference value (1.2×10^{-5} m/s^2) is maintained between 50° N and 50° S. The transitions between the different sectors are linear. In the Antarctic, results are mostly unaffected because the vertical diffusivity computed by the TKE scheme is nearly always above the default background value. Lowering the latter has therefore almost no impact in this region. Simulated mixed layer depths (MLDs) in the Arctic Ocean are reduced, leading to a better agreement with observations (Barthélemy et al., 2015).

Third, two artificial connections present in the standard version of LIM between the ice-free and ice-covered fractions of grid cells have been removed. Previously, ice was allowed to grow in the ice-free part of a grid cell only if the surface heat loss was large enough as to cool the entire top oceanic cell down to the freezing point. On the other hand, in the melting season, positive surface heat fluxes in open water were not used to increase the temperature of ocean cells in which ice was still present, but were rather transferred to the sea ice base. These two processes provided an instantaneous link between the ice-free and ice-covered parts of grid cells, and complicated the interpretation of ocean surface fluxes in open water and below ice. Their removal leads to smaller open water fractions in winter, but the combined effect on sea ice thickness is weak. The code has been modified so that ice can grow in the ice-free fraction of a grid cell as soon as the heat loss is sufficient to lower the temperature of the corresponding cell fraction to the freezing point, and positive heat fluxes in open water simply increase the sea surface temperature (SST). The impact of the treatment of ice formation in leads has been examined in greater detail in a recent study using the sea ice model CICE (Wilchinsky et al., 2015).

In virtually all large-scale applications since it was introduced in version 3 of LIM, the ITD has been used with five ice thickness categories. The surface of each grid cell is thus separated into six parts. The first one is the ice-free fraction, representing open water and leads within the sea ice cover, and the remaining five correspond to the ice thickness classes, each one having its own concentration. The upper thickness limits for the first four categories are 0.63 m, 1.33 m, 2.25 m and 3.84 m, while the fifth is unbounded. Transfers between the different categories are caused by thermodynamic growth or melt and by the deformation processes that the model accounts for, namely ridging and rafting (Vancoppenolle et al., 2009).

2.2. Ocean surface boundary conditions

Our aim here is examining the subgrid-scale heterogeneity of ocean SBCs associated with the ITD present in LIM. To this end, the surface thermohaline fluxes and the norm of the surface stress have been diagnosed separately for the six fractions of each grid cell.

On the one hand, the thermohaline fluxes are the main drivers of SST and sea surface salinity (SSS) variations, and hence of buoyancy changes at the ocean surface. We will look at the freshwater,

salt and heat fluxes, the latter being further split into its solar and non-solar components. In this study, a positive flux is directed towards the ocean. The surface stress is, on the other hand, a driver of turbulent mixing in the upper ocean. In the TKE vertical mixing scheme used in our NEMO configuration, its norm sets the surface boundary condition on turbulent kinetic energy (Madec, 2008). It is worth mentioning that, in this version of the TKE scheme, the parameterization of surface and internal wave breaking depends on the ice fraction. Since the vertical mixing computations remain unique in each oceanic columns, this does not constitute a subgrid-scale mixing scheme. The SBCs also have effects on upper ocean currents, but the impact of their heterogeneity is more complex and not discussed here.

It is important to note that these subgrid-scale fluxes and stress are merely diagnostics in this work. They are still aggregated across the six grid cell fractions before being transmitted to the ocean model. The formulation and the terms included in each of these SBC variables are detailed in the following subsections. All model features listed below are from Vancoppenolle et al. (2009) and Rousset et al. (2015) for the sea ice and from Madec (2008) for the ocean.

2.2.1. Freshwater and salt fluxes

To understand how freshwater fluxes affect the SSS in the model, it must be mentioned that our setup uses NEMO in its linear free surface formulation, with a filtering term in the momentum equation to dampen the fast external gravity waves (Roullet and Madec, 2000). This approach allows taking into account the mass flux due to freshwater input at the ocean surface in the momentum equation. However, the linearization implies that the ocean volume is fixed in time and that the thickness of the first ocean layer in particular is constant. Consequently, the salinity concentration or dilution effect associated with negative or positive (according to the convention chosen above) freshwater fluxes F_{fw} is achieved by turning them into virtual, or equivalent, salt fluxes $F_{s,v}$ following:

$$F_{s,v} = -F_{fw} S_{ss},$$

where S_{ss} is the sea surface salinity. By comparison, in a non-linear free surface context with variable volumes, such a virtual salt flux would not be necessary. In that case, the thickness of the first ocean layer would adjust to the freshwater flux and the SSS change would arise from the concentration or dilution of its unchanged salt content.

Freshwater fluxes in open water include evaporation and solid precipitation. A fraction f_0^β of all solid precipitation, with $\beta = 0.6$, reaches the open water area f_0, because winds blow some snow off the sea ice surface. In the rare cases when the air temperature is high enough to allow liquid precipitation over sea ice, these are supposed to percolate through the ice and reach the oceanic grid cell surface uniformly. Concentrating liquid precipitation in open water, in an attempt to mimic runoff from the ice, would indeed result in extremely large freshwater fluxes when the ice-free area is small. Moreover, a SSS restoring towards the PHC3 climatology (Polar Science Center Hydrographic Climatology, Steele et al., 2001) is implemented as a damping term in the surface freshwater budget, with a 310 days time scale for a 50 m mixed layer. This term is likewise spread out uniformly at the surface. It is furthermore multiplied by the open water fraction f_0, meaning that its magnitude is reduced under sea ice, as in Barthélemy et al. (2015). Finally, although continental runoffs are taken into account in the model, they are not included in the freshwater fluxes examined here.

Since the pressure effect of sea ice is not included in our model configuration, the formulation of ice-related processes implies small errors on the ocean dynamics, but their consideration is beyond the scope of the present study (e.g., Schmidt et al., 2004). As a concrete example of freshwater and salt exchanges between the ice and the ocean, the formation of sea ice at salinity S_i is associated in reality with a negative freshwater flux F^i_{fw} (out of the ocean) and with a real salt flux $F^i_{s,r}$ given by:

$$F^i_{s,r} = F^i_{fw} S_i.$$

This flux is also negative, meaning that a relatively weak amount of salt is extracted from the ocean to be stored in the sea ice. The observed increase in SSS following sea ice formation is due to the concurrent freshwater output, whose concentration effect is included, as above, by means of a virtual salt flux in the model. The total flux used to compute the SSS evolution is then:

$$F^i_s = F^i_{s,r} + F^i_{s,v} = F^i_{fw}(S_i - S_{ss})$$

and is indeed positive for sea ice formation, since $F^i_{fw} < 0$ and $S_i < S_{ss}$. Bottom growth, bottom melt, surface melt, snow-ice formation and formation of new ice in open water are handled with such a combination of real and virtual salt fluxes. The fluxes from each category and from open water are readily attributed to the corresponding grid cell fractions.

Three additional sea ice and snow processes affect freshwater and salt fluxes below each ice category. Firstly, the advanced halodynamics scheme included in LIM allows a representation of brine entrapment and drainage, and makes the sea ice salinity variable both in space and time. The rejection of brine through gravity drainage and flushing is treated as pure, real salt fluxes which are specific to each ice category. Secondly, the melt of snow accumulated on sea ice induces a pure freshwater flux to the ocean, distinct for each category. It is thus handled as a virtual salt flux in the computation of SSS. At last, ridges simulated in LIM are assumed to have a porosity of 0.3. The entrapped water volume is turned into ice with salinity $S_i = S_{ss}$, i.e. there is no immediate brine rejection. The corresponding F^i_s is zero, showing that the formation of porous ridges has no direct impact on the SSS. Subsequent brine drainage occurs nonetheless and lowers the salinity of the ridges.

What we refer to as salt flux in the following sections is actually the combination of both real and virtual components, the latter accounting for the effects of freshwater fluxes, which therefore do not need to be examined separately.

2.2.2. Heat fluxes

The solar radiation reaching the ocean surface is strongly reduced under sea ice. The high ice albedo, which in the model depends on the state of the surface, the ice thickness, the snow depth and the cloudiness, implies that a large fraction of the radiation is reflected back to the atmosphere. The remaining solar flux is totally absorbed by snow, if present. Without snow, the upper ice layer absorbs a fraction of the net surface radiation, while the rest is transmitted through the ice, where it attenuates exponentially with an attenuation length equal to 1 m. The solar heat flux considered here is the amount of energy per unit time and area that eventually reaches the ice-ocean interface. It can vary significantly from one sea ice category to another, since they have different snow covers and, by definition, different thicknesses. Inside the ocean, as parameterized in the model, 42% of the surface flux are associated to wavelengths at which seawater is more transparent. This fraction of the flux penetrates the top few tens of meters with a decreasing exponential profile and contributes to local heating. Because of a much shorter depth of extinction, the remaining 58% are absorbed in the first few meters.

The constituents of the non-solar heat flux at the ocean surface are very distinct under sea ice and in the open water. Under ice, the major contribution is the sensible heat flux from the ocean to

the ice F_w. Following McPhee (1992), it is taken to be proportional to the difference between the sea surface temperature T_{ss} and the ice base temperature, corresponding to the freezing point T_{fr} at the local salinity. It is also related to the norm of the ice-ocean relative velocity through the friction velocity u^*_{io}, whose lower bound is fixed here at 5×10^{-3} m s^{-1}. We have:

$$F_w = \rho_w c_w c_h u^*_{io}(T_{ss} - T_{fr})$$

where ρ_w is the reference seawater density, c_w the specific heat of seawater and c_h a heat transfer coefficient equal to 0.0057. Positive heat flux to the ice F_w are negative contributions to the non-solar heat flux, with our convention. They are identical for all ice categories, since the SST and SSS (hence T_{fr}) are unique within one grid cell. The non-solar heat flux at the ice-ocean interface also includes smaller terms originating from mass exchanges at temperatures different from the SST, for instance from ice or snow melt, which can vary from one category to another.

In the open water fraction of grid cells, the non-solar heat flux is made up of the atmosphere-ocean longwave, sensible and latent heat fluxes, which are computed from the classical CLIO bulk formulas described by Goosse (1997). Smaller contributions come from the sensible heat of precipitation and from the latent heat of solid precipitation. In conditions of sea ice formation, a fraction of the non-solar flux is used to erode the ocean heat content and lower the SST to the freezing point, while the remaining is compensated by the latent heat released by seawater freezing. The first component can be non-negligible in case oceanic heat is supplied from the subsurface (Haid and Timmermann, 2013). The second component does not lead to SST variations, and its effects on the water column stability are through salt fluxes associated with ice formation. In the following, we consider the first component only and refer to it simply as the non-solar heat flux, although it might not be its usual definition.

2.2.3. Surface stresses

Both the atmosphere-ocean and the ice-ocean stresses derive from quadratic bulk formulas. The drag coefficients are 1×10^{-3} and 3×10^{-3}, respectively. The norm of the ice-ocean stress is the same for all categories, since the drag coefficient is taken as a constant. More recent parameterizations allow this coefficient to be dependent on the sea ice state and therefore to evolve spatially and temporally (Tsamados et al., 2014), and could be of interest to refine the ice-ocean momentum exchange.

2.3. Experimental design

The model simulation is designed as follows. The initial temperature and salinity fields are taken from the World Ocean Atlas 2001 (Conkright et al., 2002), and the ocean-sea ice model is run from January 1948 until December 2014. Atmospheric forcing fields consist of a combination of NCEP/NCAR daily reanalysis data of surface air temperature and wind speed (Kalnay et al., 1996) with monthly climatologies of relative humidity (Trenberth et al., 1989), cloudiness (Berliand and Strokina, 1980) and precipitation (Large and Yeager, 2004). Continental runoff rates are prescribed from the climatological dataset of Dai and Trenberth (2002). In the Antarctic, a runoff of 2600 Gt year^{-1} is distributed over the grid boxes closest to the continent, with a seasonal cycle presenting a maximum in December and a minimum from June to August. Heat fluxes at the atmosphere-ice and atmosphere-ocean interfaces are parameterized as in Goosse (1997).

The ocean and sea ice models run over a common domain extending from 78° S to 90° N. This domain is discretized on the quasi-isotropic global tripolar grid ORCA1, based on the semi-analytical method of Madec and Imbard (1996), which has 1° resolution in the zonal direction. A z coordinate is used on the vertical.

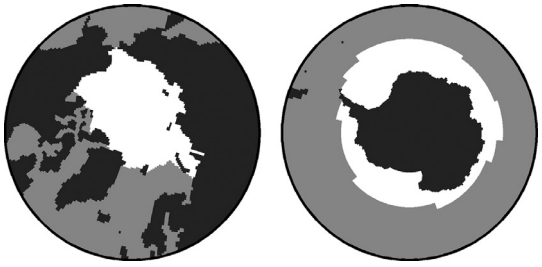

Fig. 1. Selected areas for the computation of mean seasonal cycles.

The surface layer is 6 m thick. The thickness of the 46 layers increases non-uniformly with depth, reaching 20 m at 100 m depth and 250 m for the bottommost layer. The ocean model has a time step of 1 h and LIM is called every six ocean time steps.

3. Results: sea ice

Results from our NEMO-LIM simulation are now examined, starting with the overall state of the sea ice and the ITD. Except when compared to specific observational datasets, the last 20 years (1995–2014) of the outputs are analyzed. The 47 year spinup (1948–1994) in the single cycle of the NCEP/NCAR reanalysis that we run is sufficient for the sea ice and upper ocean to adjust to the forcing. It is therefore also appropriate for the analyses of SBCs that we want to conduct.

In this section and the following, mean seasonal cycles of spatially-averaged model fields are shown. In both hemispheres, the domain chosen for the averaging is the intersection between the regions depicted in Fig. 1 and the areas where the monthly mean sea ice concentration exceeds 15%. During the summer months, the 15% threshold is more restrictive. It is required to avoid including areas of very low ice concentrations, where the considered fields tend to depart very strongly from the values they have elsewhere. During the winter season, the domain is rather constrained by the regions selected in Fig. 1, which are chosen in order to ensure that the average values are typical of the inner sea ice pack. The Arctic area includes the Arctic Ocean and the marginal seas, excluding the Barents Sea and with boundaries at Bering Strait, the northern limit of the Canadian Arctic Archipelago (CAA) and Fram Strait. Without an obvious physical northern boundary, the Antarctic area is based on a visual examination of the position of the simulated winter sea ice edge. The conclusions derived from the mean seasonal cycles shown in Figs. 2, 6 and 10 are qualitatively insensitive to the details of the areas chosen above. Quantitatively, however, one has to keep in mind that these figures represent the situation for the inner sea ice pack.

The 15% ice concentration threshold further implies that the sea ice edge is systematically excluded from the computation of mean seasonal cycles. While we will not study this part of the sea ice cover in details, the spatial distributions presented in Figs. 3, 7, 8, 9 and 11 are not masked but show the mean 15% ice contours, allowing to visualize how the ice edge differs from the rest of the pack. These maps are shown for February and July in the Northern Hemisphere (NH) and for January and August in the Southern Hemisphere (SH). These months have been found to be the most representative of the winter situation immediately prior to the sea ice extent maximum (February and August) and of the summer season (July and January) for the various fields that we examine.

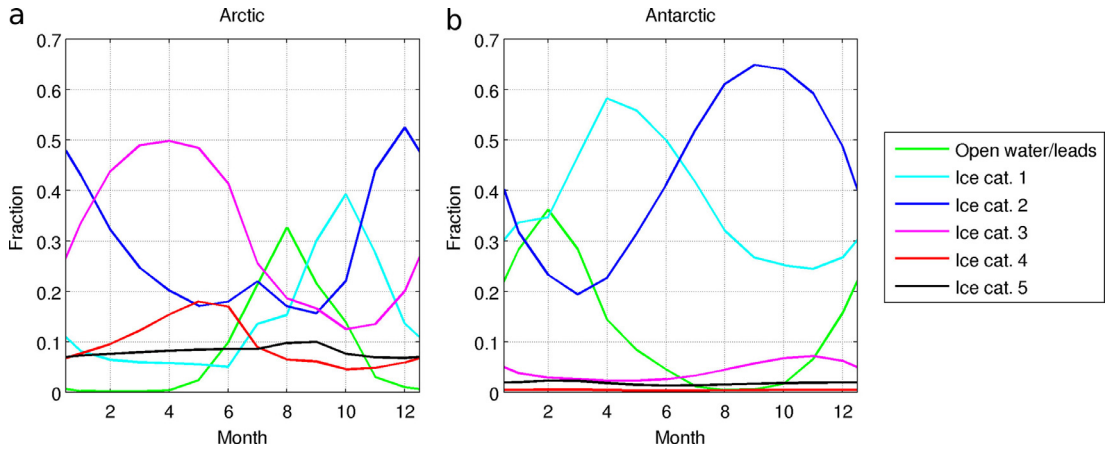

Fig. 2. Seasonal cycles of simulated fractions of grid cells covered by open water/leads and by ice categories, averaged in the areas depicted in Fig. 1 and where sea ice concentration exceeds 15%, in the Arctic (a) and the Antarctic (b). The upper bounds for the first four ice thickness categories are 0.63 m, 1.33 m, 2.25 m and 3.84 m. The fifth category is unbounded.

Table 1
Sea ice metrics in observations or reanalyses and as simulated by the model. Sea ice extent is compared between 1983 and 2012 with passive microwave products generated with the Bootstrap algorithm (Comiso, 2000). Arctic sea ice volume estimates are from the PIOMAS reanalysis (Schweiger et al., 2011) over the 1983–2013 period. The Antarctic sea ice volume data are from the model reconstruction by Massonnet et al. (2013) between 1980 and 2008.

	Arctic		Antarctic	
	Obs./reanalysis	Model	Obs./reanalysis	Model
Max. monthly extent (10^6 km^2)	15.5	17.1	19.2	20.8
Min. monthly extent (10^6 km^2)	6.7	7.9	3.2	7.6
Trend extent (10^3 km^2 year^{-1})	−53	−56	+21	+28
Max. monthly volume (10^3 km^3)	27.8	33.0	10.1	16.2
Min. monthly volume (10^3 km^3)	11.2	17.4	1.9	4.7
Trend volume (km^3 year^{-1})	−346	−361	+36 ± 34	+60

3.1. Overall view

In Table 1, general sea ice metrics are given that allow to compare the model results with observations.

Arctic sea ice extent is slightly overestimated compared to passive microwave products generated with the Bootstrap algorithm (Comiso, 2000). The positive bias is larger in winter and is comprised between 1 and 2 $\times$ 10^6 km^2 throughout the year. The declining trend over recent decades is in excellent agreement with observational estimates. While absolute values of ice volume appear significantly larger than the PIOMAS reanalysis using data assimilation (Schweiger et al., 2011), the amplitude of its mean seasonal cycle is very similar, as is its interannual trend. The differences in total volume can be shown to originate from the CAA, whose representation by the model is challenging at 1° resolution and where thick stagnant ice accumulates in LIM.

The positive bias in sea ice extent in the Antarctic is larger than in the NH, most importantly in summer when the observed extent is less than half the simulated one. This seems to be caused by an inability to melt ice rapidly enough during spring in the simulation. This issue was already present in studies using older versions of LIM with a similar atmospheric forcing (CLIO bulk formulas, Massonnet et al., 2011; Lecomte et al., 2013), but is absent in a more recent configuration where another forcing formulation is used (CORE bulk formulas, Rousset et al., 2015). The excessive summertime ice cover is located mostly in the eastern Weddell Sea, and to a lesser degree in the Ross and Amundsen Seas. This is the main discrepancy between model results and available observations, which has to be kept in mind when analyzing other aspects of the simulation. It is also associated with a positive bias in sea ice volume compared to the model reconstruction with data assimilation of Massonnet et al. (2013). Interestingly, the simulated trend in Antarctic ice extent is comparable with satellite estimates, whereas the volume trend in LIM lies within the range provided by Massonnet et al. (2013).

3.2. Ice thickness distribution

Mean seasonal cycles showing the behavior of the ITD in LIM are presented in Fig. 2. In both hemispheres, the mean open water fraction falls very close to zero in winter and peaks between 0.3 and 0.4 in summer. As a reminder, these values are obtained from an averaging inside the sea ice pack by excluding areas with less than 15% concentration. The amplitude of the seasonal variations of ice categories fractions tends to decrease with increasing thickness. This is more striking in the SH where the third category already has a very weak seasonal cycle. The distribution across the different classes is also very distinct in the Arctic and the Antarctic. In the former, all categories contribute notably to the total sea ice concentration, while in the latter the first two ice classes are clearly dominant, with a smaller contribution from the third one in winter. A recent study has shown that having five categories in an ITD may not be enough to provide an accurate representation of the Arctic sea ice cover (Hunke, 2014). The issue is therefore likely even more critical in the SH. Thin ice forms as the freezing season begins, before being progressively replaced by thicker ice, either from thermodynamic growth or from deformation processes. This evolution is visible in the mean seasonal cycles. Starting in

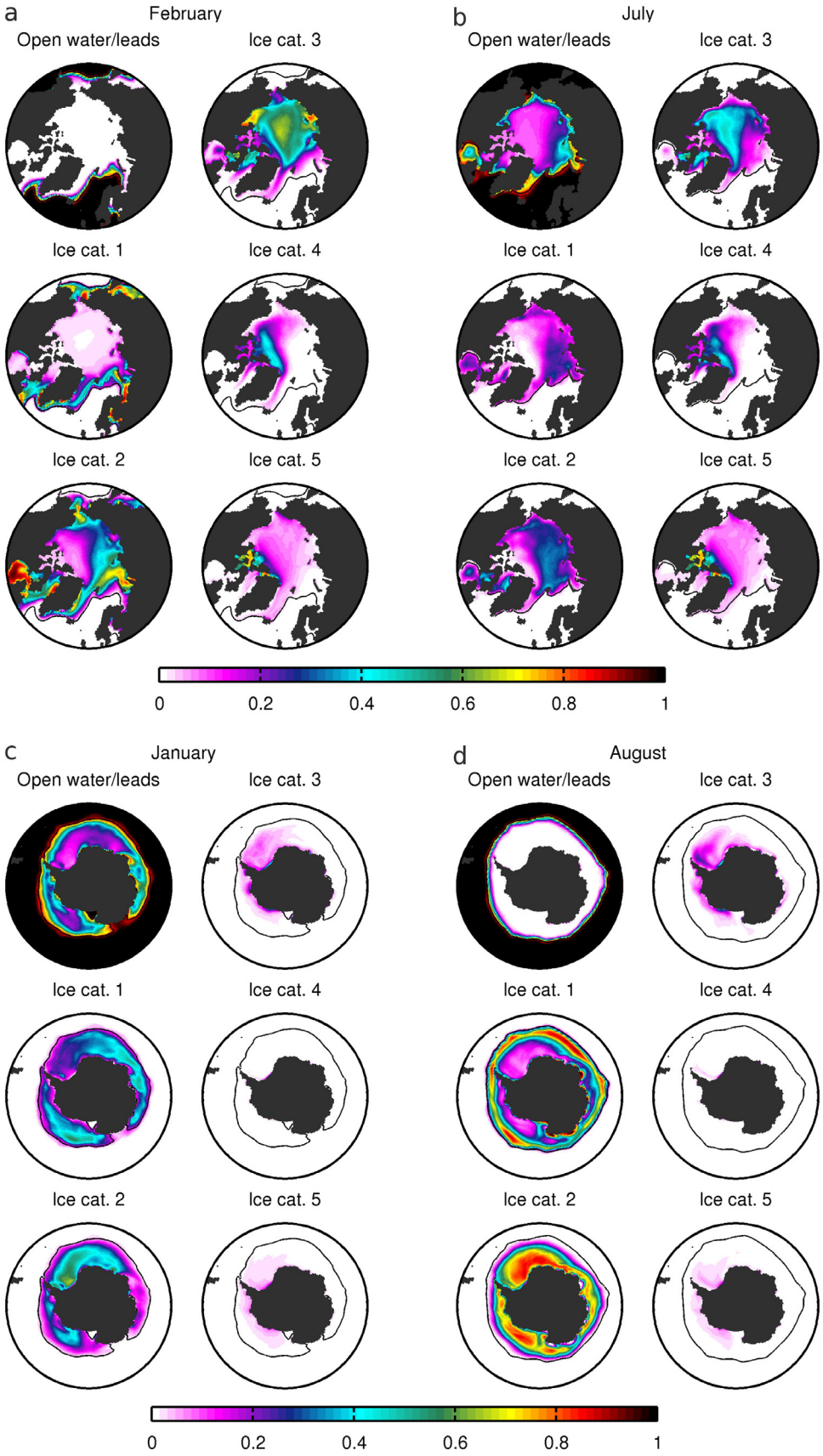

Fig. 3. Simulated fractions of grid cells covered by open water/leads and by ice categories, for February (a) and July (b) in the Arctic and for January (c) and August (d) in the Antarctic. The black lines correspond to the 15% ice concentration contours.

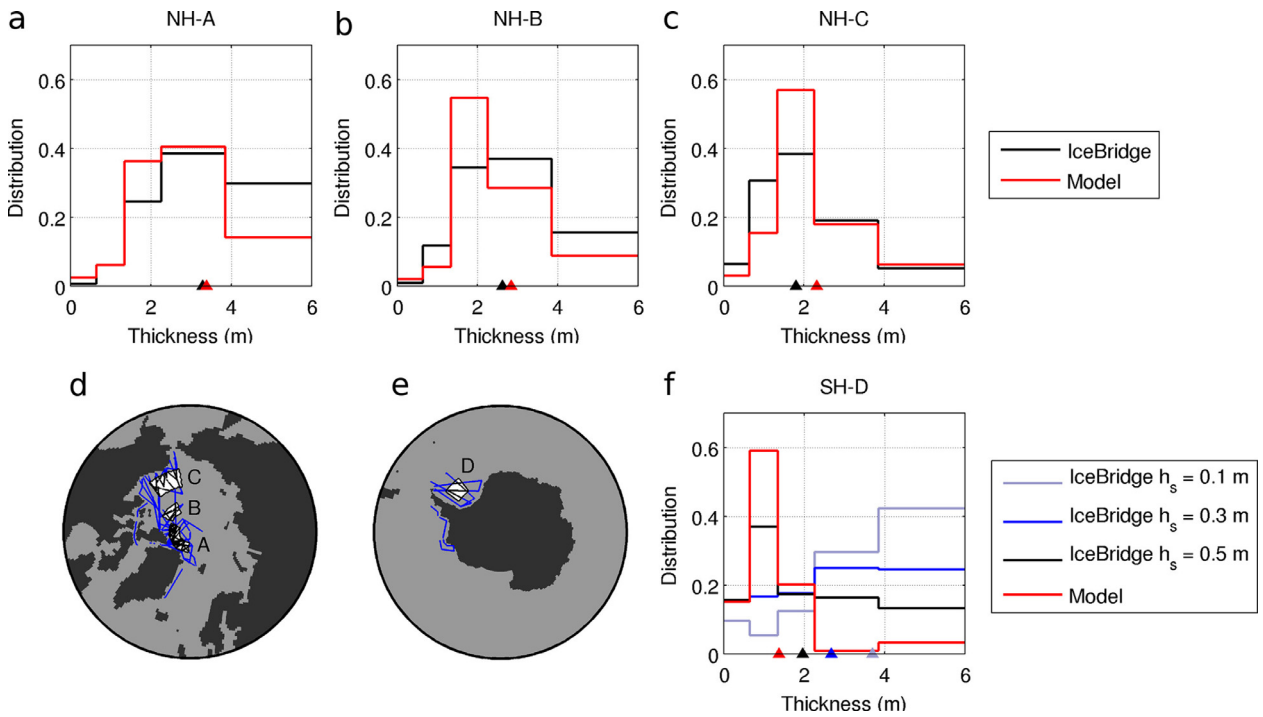

Fig. 4. Ice thickness distribution in selected areas (delineated on the maps, d, e) in the IceBridge dataset and in the model, averaged in March and April between 2009 and 2013 in the Arctic (a, b, c) and in October between 2009 and 2010 in the Antarctic (f). The triangles on the *x*-axis indicate the mean ice thickness in those areas. The three IceBridge curves on the SH plot correspond to different hypotheses regarding the snow depth onto sea ice (h_s, see text for details). The numbers of IceBridge data points used in NH-A, NH-B, NH-C and SH-D are 317 534, 55 069, 113 854 and 74 053, respectively.

summer, the months of the maximum mean fraction of each ice class are indeed exactly ordered according to their thickness.

Fig. 3 shows that the distribution among ice categories is extremely variable in space. In February in the NH, high concentrations in the first and second ice categories are confined along the sea ice edge and in the marginal seas and eastern part of the Arctic basin, respectively. Most of the Arctic Ocean is occupied by ice in the third thickness category, with large values in the fourth and fifth ones north of Greenland and in the CAA. In July, extensive areas are still covered with ice in the third class, while the concentration of the first one has increased in the central part of the basin as a result of melting of thicker ice.

The same distinctions among the categories can be observed in the SH. In winter, thin ice is present in the northernmost regions, but also in coastal areas (mostly in the Ross Sea and along the coast of East Antarctica), where strong offshore winds transport ice northwards, creating polynyas and reducing the mean ice thickness (e.g., Barthélemy et al., 2012; Nihashi and Ohshima, 2015). Thicker ice in the inner sea ice pack is represented mostly by the second category, and to a small extent by the third one in the Weddell, Bellingshausen and Amundsen Seas. In summer, the open water fraction is more variable than in the Arctic, with large values in the regions of thin winter ice, especially in the Ross Sea polynya.

The large-scale validation of a modeled ITD is a complex task. Nonetheless, the measurements collected during Operation IceBridge campaigns provide a way to carry out a model-observation comparison in specific seas and regions with sizes of the order of 500 km. Datasets obtained during airborne surveys from an array of remote sensing platforms have been processed to retrieve sea ice freeboard and snow depth, from which ice thickness is derived based on a hydrostatic balance assumption (Kurtz et al., 2013). Two separate datasets are utilized here. The first one, which has been reprocessed very recently, includes data collected mostly in the American side of the Arctic Ocean from 2009 to 2013 in the months of March and April (Kurtz et al., 2015). The second includes measurements from two campaigns in October of the years 2009 and 2010, primarily in the Weddell Sea (Kurtz et al., 2012).

IceBridge data are given at 40 m resolution in the along-track direction. We compute the observed ITD by constructing histograms with thickness ranges corresponding to the LIM ice thickness categories. The simulated ITD is taken as the five ice classes average concentrations. Because of this difference in the way mean ITDs are computed, large spatial gradients in sea ice properties could make the model-data comparison questionable. In order to minimize the issue, the analysis is carried out in limited areas where the IceBridge data coverage is high (Fig. 4). Three areas are selected in the Arctic: north of Greenland and the CAA (NH-A, 84-87° N, 5-115° W), in the northern part of the Canada Basin (NH-B, 81-84° N, 120-155° W) and north of Alaska (NH-C, 72-77° N, 140-170° W). The data from March and April are aggregated. In the SH, a single area in the Weddell Sea is considered (SH-D, 68-73° S, 38-53° W). Nevertheless, the retrieval of snow depth from the radar system for the Antarctic region is still highly uncertain (Kurtz et al., 2013). As a consequence, only sea ice freeboard is provided in the IceBridge dataset. We crudely assume three uniform snow depths of 0.1, 0.3 and 0.5 m, to obtain an uncertainty range in the ice thickness recovered from hydrostatic balance. The range in snow depth is likely sufficiently wide to include a realistic estimate (Lecomte et al., 2013). For points where the assumed snow thickness is larger than the measured freeboard, it is reduced to be equal to the latter. In the end, several tens of thousands thickness data points can be used in each region.

The ITDs derived from observations and from the model are shown in Fig. 4. In the Arctic, the overall shape of the distribution is well reproduced, exhibiting in each region a dominance of intermediate ice thicknesses over thin and thick ice types. Yet, quantitatively, large differences occur with IceBridge estimates. In NH-A, the model lacks 50% of the ice thicker than 3.84 m. In the other two Arctic areas, the ice is too concentrated in the third category, at the expense of almost all other ones in NH-B, or of only

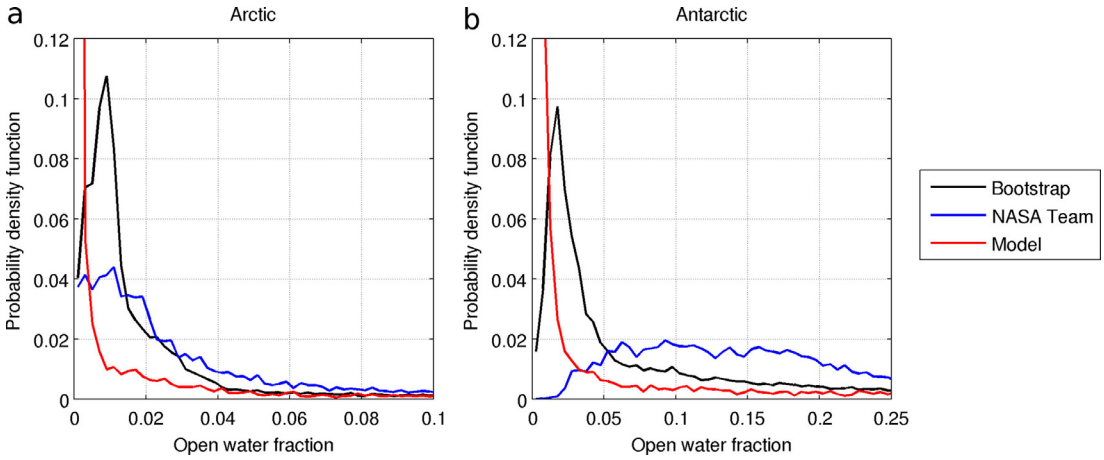

Fig. 5. Probability density functions of the winter open water fraction, for the Bootstrap (Comiso, 2000) and NASA Team (Cavalieri et al., 1996) satellite products and for our model simulation, on average over the 2001–2010 period, for March in the Arctic (a) and for September in the Antarctic (b).

the thinner ones in NH-C. The apparent good agreements between simulated and observed mean thicknesses are therefore achieved through a representation of the ITD that is reasonable but still displays clear biases. Errors up to 50% in specific category concentrations are indeed not uncommon. It is worth noting however that the IceBridge ice thicknesses have a large uncertainty, of the order of 75 cm on average in the NH areas considered (Kurtz et al., 2015).

In the SH, the absence of snow measurements prevents a detailed model-observation comparison. Nonetheless, whatever the assumed snow depth, too much ice lies in the second category, while ice above 2.25 m appears critically missing from the modeled ITD. The processing of the IceBridge measurements includes a filter designed to remove the data contaminated by icebergs (Kurtz et al., 2012), which hence cannot explain this discrepancy. We note a negative bias in the simulated mean ice thickness in SH-D, that is specific to this region. Except in a few coastal areas, LIM in this configuration actually overestimates the Antarctic sea ice thickness compared to the ASPeCt dataset based on shipboard observations (Antarctic Sea ice Processes and Climate, Worby et al., 2008), with a mean absolute error of 45 cm.

A comparison of the observed and simulated winter open water fractions is finally presented in Fig. 5, over a common and longer period for both hemispheres (2001–2010). Results are qualitatively insensitive to the chosen winter months. A large spread exists between the probability density functions obtained for the Bootstrap (Comiso, 2000) and NASA Team (Cavalieri et al., 1996) algorithms, although they utilize the same passive microwave datasets. These uncertainties in the observational estimates illustrate the difficulties to derive accurately low open water fractions from satellite measurements. The differences between the two products are especially large in the Antarctic, where the NASA Team algorithm yields much lower sea ice concentrations. In any case, the simulated open water fractions seem strongly underestimated in winter in both hemispheres. This is related either to a lack of ice divergence in the model, or to an excessively rapid closing of leads. The bias likely reaches a few percent in the Arctic and is as large as 10 to 15% in the Antarctic if the NASA Team product is considered.

4. Results: ocean surface boundary conditions

The discussion in the previous section has demonstrated that the simulated concentrations in open water and in ice thickness categories differ quantitatively from reality. In the detailed examination of SBCs that follows, we will thus mostly focus on the thermohaline fluxes and surface stress for the six parts of grid cells separately, regardless of their areal fraction. In other words, the spatially averaged seasonal cycles are computed without weighting the fields by the concentrations of the open water and ice categories, in order not to be impacted by errors in the modeled ITD. The contribution of a specific portion of the surface to the total flux or stress is also of interest to estimate to which extent it participates in the forcing of the ocean. But these mean contributions depend on the areal fractions of open water and ice categories, whose representation in the simulation is uncertain. This aspect will consequently be only briefly addressed in Section 4.4.

4.1. Salt fluxes

The mean seasonal cycles of salt fluxes are shown in Fig. 6 and the geographical distributions are presented in Fig. 7. In winter, the most intense ice production rates take place in leads. Their salt fluxes are at least one order of magnitude larger than those of any ice category. They reach almost 0.05 and 0.04 kg PSU m^{-2} s^{-1} on average in the Arctic and Antarctic, respectively. To put these values in perspective, the growth, over the course of one month, of 1 m of ice whose salinity is 30 PSU lower than the SSS would correspond to a salt flux of 0.01 kg PSU m^{-2} s^{-1}. In one month, such a flux would increase the salinity of a 50 m mixed layer by 0.5 PSU. Fluxes of large magnitude are widespread across the Arctic basin and their values tend to decrease towards lower latitudes and towards the sea ice edge, where air is less cold. In the SH, the largest fluxes are essentially found in a narrow band around the continent. Exceptions are the northern tip of the Antarctic Peninsula, as well as a central part of the Ross Sea and an area west of the Amery Ice Shelf, where sea ice production is counteracted by high oceanic heat supply (Fig. 9).

The freezing rate below existing ice is determined by the balance between the oceanic and conductive heat fluxes. Since the latter is inversely related to ice thickness while the former is identical for all categories, more ice forms under the thinner classes. Other factors contributing to this relation include a shallower depth of insulating snow on young thin ice and, in the Antarctic, more frequent snow-ice formation for thin ice that cannot support a lot of snow. Decreasing salt fluxes for categories of increasing thickness are indeed visible in model results (see also the equivalent of Fig. 6 in the supplementary material, in which the axes have been adjusted in order to better visualize the differences

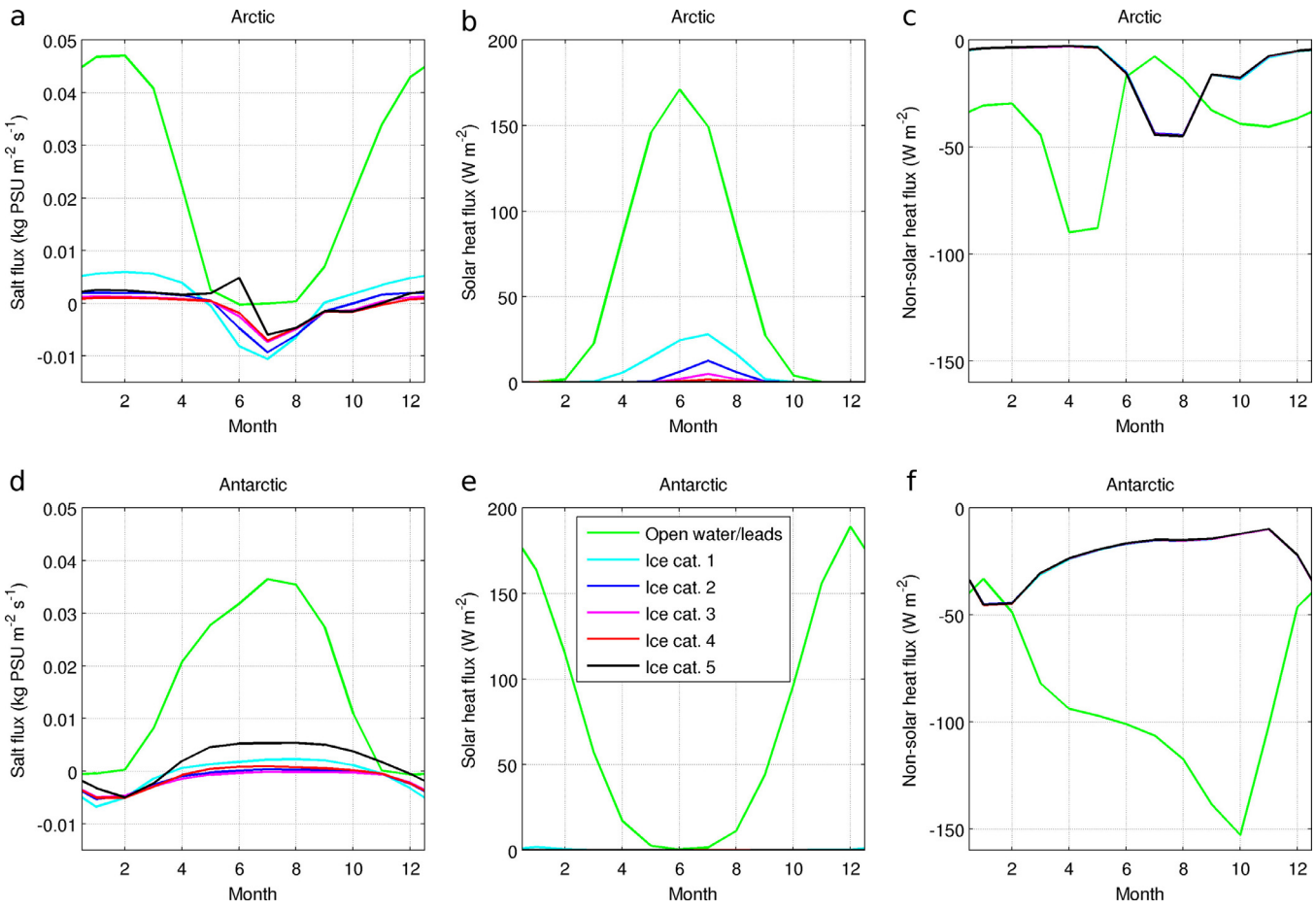

Fig. 6. Seasonal cycles of simulated salt (a, d), solar heat (b, e) and non-solar heat (c, f) fluxes in open water/leads and under ice categories, averaged in the areas depicted in Fig. 1 and where sea ice concentration exceeds 15%, in the Arctic (a, b, c) and the Antarctic (d, e, f). Positive fluxes are directed towards the ocean. The solar heat fluxes in the Antarctic are very close to zero for all ice categories, whereas the non-solar heat flux seasonal cycles are nearly identical for all categories.

between the ice categories). The relation breaks in the Arctic seasonal ice zone and in the Antarctic for the fourth and fifth categories. In those regions, very thick ice is only produced by ridging, which incorporates large amounts of salt. The effect of later brine drainage is to yield positive salt fluxes, up to 0.02 kg PSU m^{-2} s^{-1} locally, even though such ridges may be so thick as to melt from below throughout the year. This process occurs, however, for very small concentrations. Finally, for all categories and both hemispheres, sea ice advected close to or across the ice edge is melting, hence freshening the ocean, even during the coldest winter months.

In summer, the salt fluxes in the open water and leads are very low, reaching a minimum of the order of $-5\ 10^{-4}$ kg PSU m^{-2} s^{-1} on average in both hemispheres. They actually only comprise the effects of evaporation and precipitation, since no explicit lateral melt is implemented in LIM. Besides, no runoff from the snow and ice surface melt is assumed. This is a physical shortcoming of the model, but determining the fraction of the meltwater that flows onto the ice surface and reaches the open water is a non-trivial question. This is also related to the representation of melt ponds, which are absent from this version of LIM but have been examined recently (Lecomte et al., 2015).

Negative salt fluxes from ice melt are larger in magnitude than the positive fluxes from ice growth, but the melt season is shorter than the growth season so that the two nearly compensate in an annual mean. Summer fluxes are of the order of -0.01 kg PSU m^{-2} s^{-1} in the NH and -0.005 kg PSU m^{-2} s^{-1} in the SH. The differences among the ice categories show that the melt rate varies from one to the other as well. Thin ice loses its snow cover more rapidly, which increases its albedo and its surface melt. In July in the Arctic, the ocean freshens almost twice as fast under the first category than under the fifth. The peak in salt flux for the fifth ice class in June is due to brine flushing favored by increasing ice temperatures and meltwater input at the surface. The largest freshening occurs along the sea ice edge, where air temperatures are high and where the ocean is strongly warmed by solar radiation entering large open water areas.

4.2. Heat fluxes

Simulated solar heat fluxes are shown in Figs. 6 and 8. The mean seasonal cycle for the open water portion of grid cells is mostly driven by the strong seasonality of insolation in polar regions. To a small extent, these cycles can be modulated by changes in cloudiness, whose importance is clearly visible in the spatial distribution. In the Arctic, solar radiation at the ocean surface is essentially zero from October to February and peaks at 170 W m^{-2} in June. The mean solar heat flux in the SH area that we have chosen for analysis (Fig. 1) is close to zero only from May to July, because it extends to lower latitudes. The maximum insolation of 190 W m^{-2} occurs in December.

As a reminder, for the ice-covered fractions of grid cells, what we consider is the penetrative shortwave flux that reaches the base of the ice. As explained in Section 2.2.2, the amount of solar energy transmitted through sea ice depends not only on its thickness, but also on the state of the snow cover and of the ice surface. In

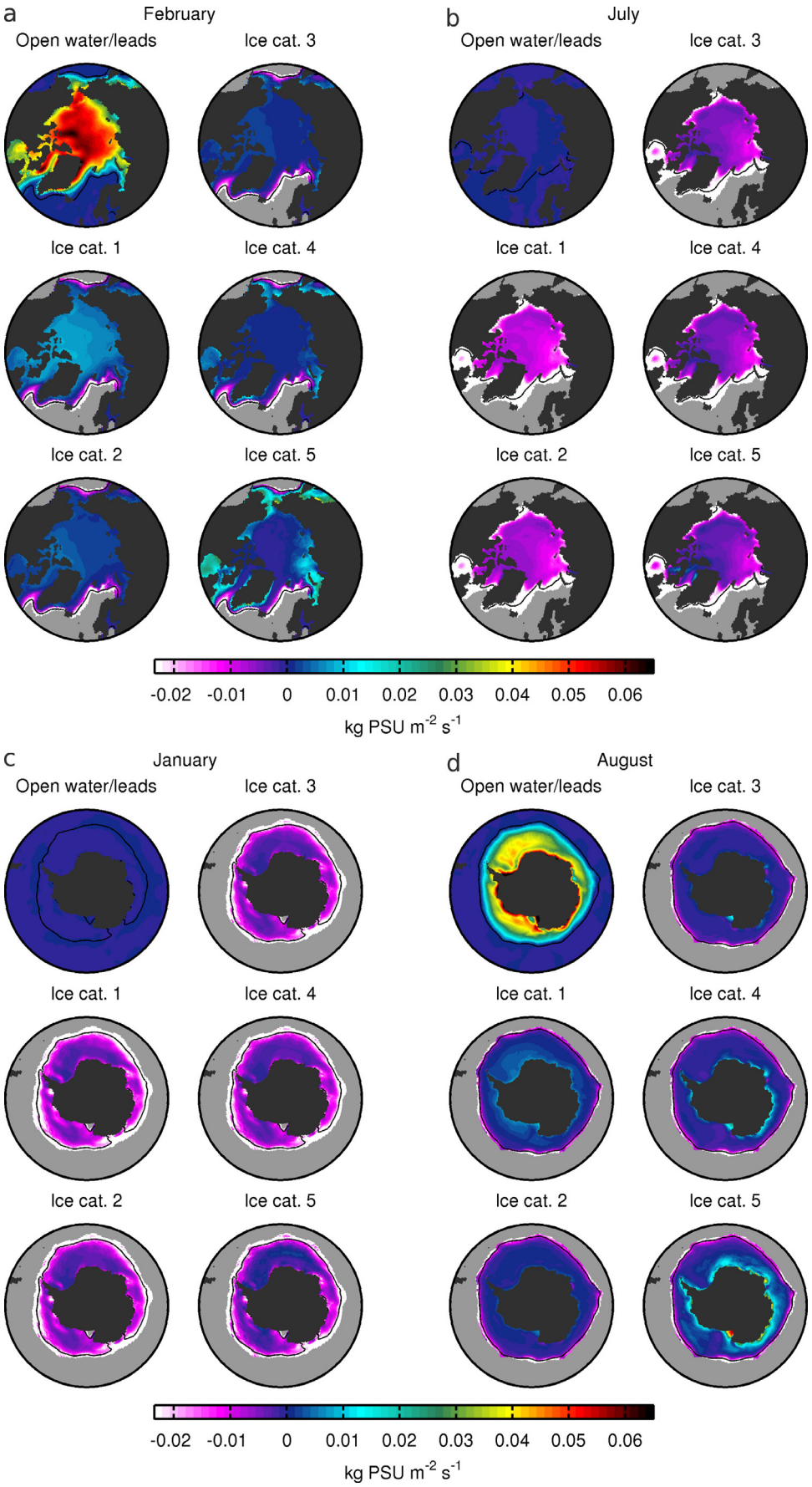

Fig. 7. Simulated salt fluxes in open water/leads and under ice categories, for February (a) and July (b) in the Arctic and for January (c) and August (d) in the Antarctic. The black lines correspond to the 15% ice concentration contours.

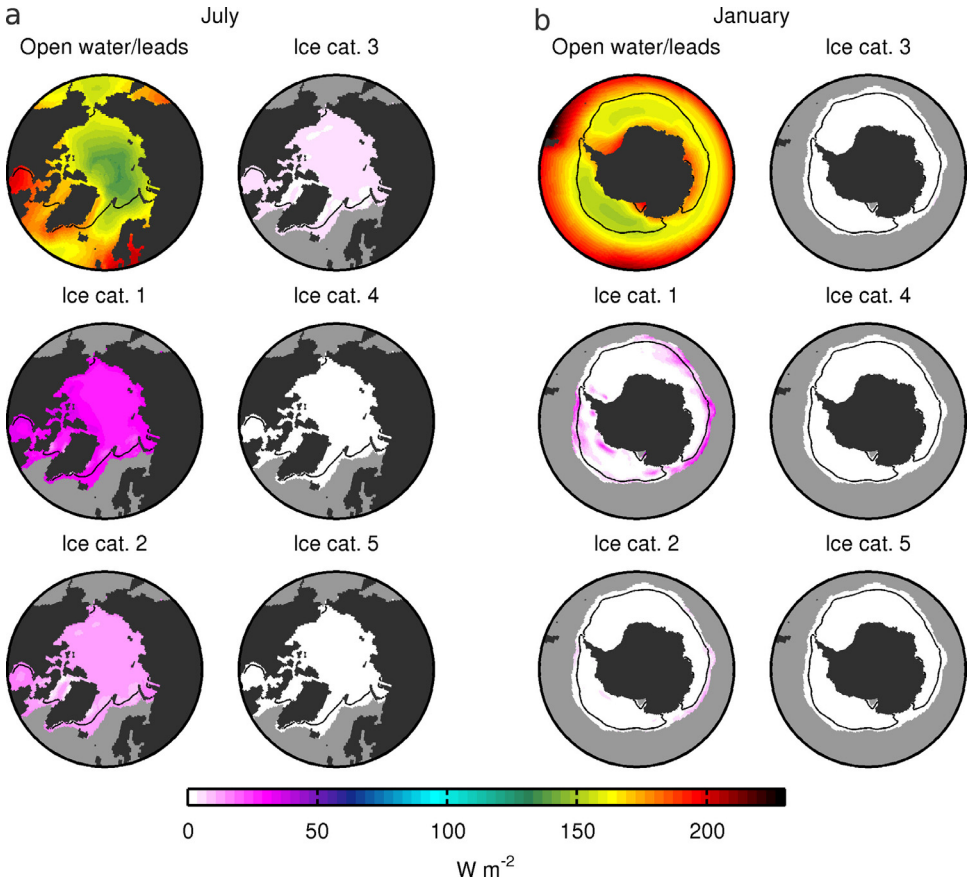

Fig. 8. Simulated solar heat fluxes in open water/leads and under ice categories, for July in the Arctic (a) and for January in the Antarctic (b). The black lines correspond to the 15% ice concentration contours.

our simulation, Antarctic sea ice remains snow-covered throughout summer, except the first category in limited areas along the edge and in the Amundsen Sea. There, up to 25 W m^{-2} is transmitted through the first sea ice category. However, when averaged over the entire ice pack as in Fig. 6, the numbers become much smaller. Thus, in the model, little solar radiation appears to reach the Southern Ocean from the ice, although this claim could be affected by its positive summer ice bias.

The situation is different in the Arctic. Except very locally for the thickest ice, snow melts away during summertime. The peak in transmitted solar heat results from both the changes in surface conditions and the general increase in insolation. Expectedly, more radiation enters the ocean earlier in the season through thinner ice. The maximum occurs in July with values of 28, 13 and 5 W m^{-2} on average for the first three categories, while being negligible for the thickest two (see also the equivalent of Fig. 6 in the supplementary material). This is slightly later than suggested by the results of Arndt and Nicolaus (2014), whose observation-based estimates indicate a maximum monthly mean solar heat flux under ice in June, with 96% of the annual input taking place between May and August. Using under-ice measurements taken mainly in August 2011, Nicolaus et al. (2012) find a threefold increase in transmitted solar radiation between first-year ice and multi-year ice. The ratios between the solar heat flux in August under the first category and the second, third and fourth ones are 3, 9 and 27, respectively. Under the assumption that thicker ice is older, this might suggest too large a gradient in transmitted solar energy in the model. Finally, energy budget measurements of a melting ice floe 0.8 m thick north of Svalbard in July and August 2012 give a transmitted heat flux through ice of 26 W m^{-2} (Hudson et al., 2013). Simulated solar fluxes for the corresponding region and period range between 10 and 15 W m^{-2} for the second ice category, whose thickness interval (0.63 to 1.33 m) encompasses that of the observed floe. A better agreement is found with the thinner first category, whose fluxes lie between 20 and 30 W m^{-2}.

The mean seasonal cycles of non-solar heat fluxes are plotted in Fig. 6. As mentioned in Section 2.2.2, differences among the sea ice categories can only originate from heat fluxes associated with mass exchanges in the model. It turns out that the fluxes for the different categories are practically indistinguishable. This means that the only significant contribution is the oceanic heat flux to the ice base, which is uniform in each grid box. Only the first category is therefore represented in the spatial distributions shown in Fig. 9. In contrast to the solar component of the surface heat flux, the non-solar part always acts to cool the ocean.

Seasonal changes in ocean-to-ice heat flux are mostly driven by SST variations because the ice base temperature is fixed at the freezing point, which does not vary much. Maxima (in absolute values) occur in both hemispheres just after the peak in insolation, i.e. in July and August in the NH and in January and February in the SH. The oceanic heat loss to the ice is around 45 W m^{-2} on average during these months. As insolation vanishes and the solar heat stored in the ocean decreases, the oceanic heat flux diminishes, reaching minima of 3 W m^{-2} in April in the Arctic and 10 W m^{-2} in November in the Antarctic, on average. At those times, the ocean surface is maintained above the freezing point mainly due to entrainment of warmer water from below. The very low value in the NH is consistent with the view that, at least away from shallow bathymetric features, heating of the Arctic mixed layer mostly originates in summer solar heating (Maykut and McPhee, 1995; McPhee et al., 2003).

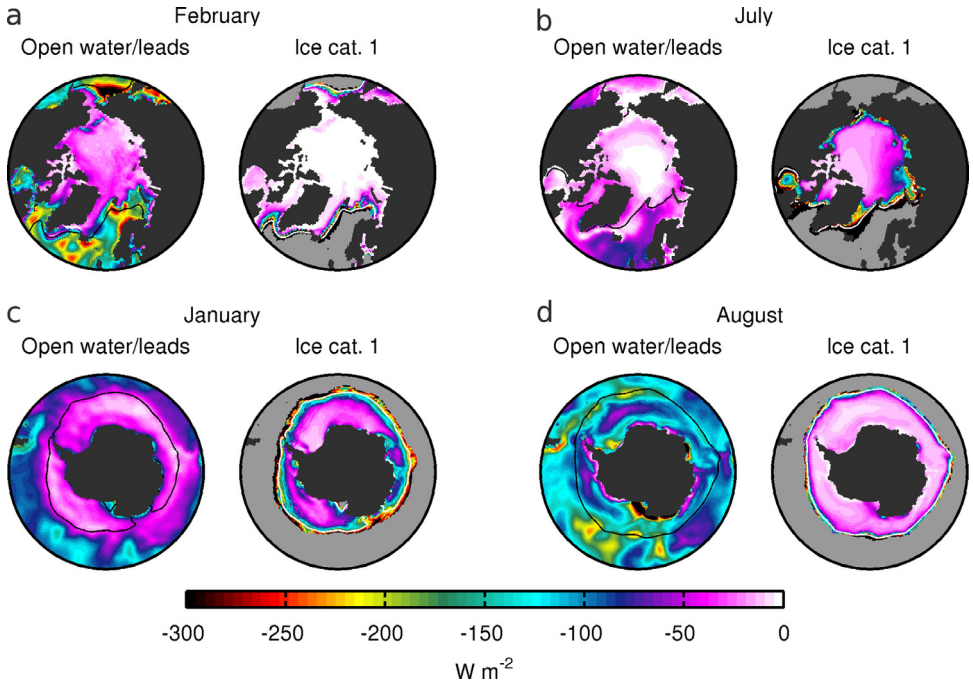

Fig. 9. Simulated non-solar heat fluxes in open water/leads and under the first ice category, for February (a) and July (b) in the Arctic and for January (c) and August (d) in the Antarctic. The black and the white lines correspond to the 15% ice concentration contours.

As shown in Fig. 9, strong spatial variations exist, which complicates the comparison between the existing local observations and the simulated average values given above. Higher heat fluxes are encountered in winter in peripheral regions where a longer ice-free season allows more solar energy to enter the ocean (Hudson Bay, for instance) and along the ice edge where sea ice is advected in warm waters. In summer, intense oceanic heat fluxes are associated to large open water fractions and reach several hundreds W m^{-2} in low ice concentration areas.

In the Arctic, the high mean summertime value of 45 W m^{-2} arises partly from the large fluxes in the low ice concentration regions. Based on data collected between 2002 and 2010 in the Transpolar Drift in the framework of the North Pole Environmental Observatory, Stanton et al. (2012) obtained a lower maximum ocean-to-ice heat flux of around 15 W m^{-2} from mid-July to the end of August. In their energy budget analysis of a melting ice floe in the Nansen Basin in July and August 2012, Hudson et al. (2013) found that the oceanic turbulent heat flux provided, on average, 13 W m^{-2} of energy to the ice. Measurements from the SHEBA study (Surface Heat Budget of the Arctic Ocean) in 1997 and 1998 showed a heat flux as low as a few W m^{-2} from October through June, followed by a steady increase reaching a peak value of about 33 W m^{-2} in July (Perovich and Elder, 2002). Results from the AIDJEX campaign (Arctic Ice Dynamics Joint Experiment) in 1975 in the Beaufort Sea also found the heat flux from the ocean to the ice to be strongly seasonal, with maximum values of 40 to 60 W m^{-2} in August (Maykut and McPhee, 1995). A comparison with the synthesis by Krishfield and Perovich (2005) ultimately confirms the good observation-model agreement, at least qualitatively, at the scale of the Arctic basin (Fig. 5 in the above-mentioned reference).

Oceanic heat flux measurements are even rarer in the Antarctic. Observations collected during the Austral winter in 1994 in the Weddell Sea near Maud Rise yielded fluxes between 25 and 35 W m^{-2} (McPhee et al., 1999). Mixed layer turbulence data obtained during two wintertime drift stations in August 2005 in the same region gave average fluxes of 13.8 and 28.0 W m^{-2} (Sirevaag et al., 2010). By comparing sea ice thickness observed using upward-looking sonars with simulations of thermodynamic sea ice growth in the central Weddell Sea, Behrendt et al. (2015) noted that the best consistency between observations and model results was obtained for average oceanic heat fluxes between 6 and 14 W m^{-2}. Except for this later, indirect, source of information, the mean seasonal cycle in Fig. 6 and the spatial distributions in Fig. 9 appear compatible with the extremely sparse observations.

The non-solar component of the surface heat budget is significantly different in the open water compared to the ice-covered fraction of the grid cells. The heat loss at the water surface depends on both the SST and the state of the atmosphere. Minima are reached in summer, about at the same period ocean-ice fluxes are at their maximum, in absolute value. The mean in the regions considered for the computation of seasonal cycles is as low as -8 W m^{-2} in the Arctic and -30 W m^{-2} in the Antarctic. As already explained, during the freezing season, the total heat loss from the ocean to the atmosphere is used partly to cool the ocean and partly to compensate latent heat released by sea ice production, and the flux considered here corresponds to the first component only. Very low values simulated in the Antarctic in winter along the coast of the Amundsen and Bellingshausen Seas and of most of East Antarctica indicate that the ocean there is close to the freezing point and that almost all of the heat loss is used to form ice. On the contrary, large fluxes are found in the Weddell Sea (< -200 W m^{-2}) and in and west of the Ross Sea and west of the Amery Ice Shelf (< -300 W m^{-2}), which are the signs of a strong energy supply from the subsurface. On average, the non-solar heat flux becomes higher over the course of the freezing season, as the deepening of the mixed layer entrains larger amounts of heat, reaching -90 W m^{-2} in April in the NH and -150 W m^{-2} in October in the SH. The increase is relatively steady in the Antarctic, whereas in the Arctic, it first settles at an intermediate value between -30 and -40 W m^{-2} from September to February. A more detailed examination of its various components would be needed to fully understand this behavior. The smaller value in the Arctic

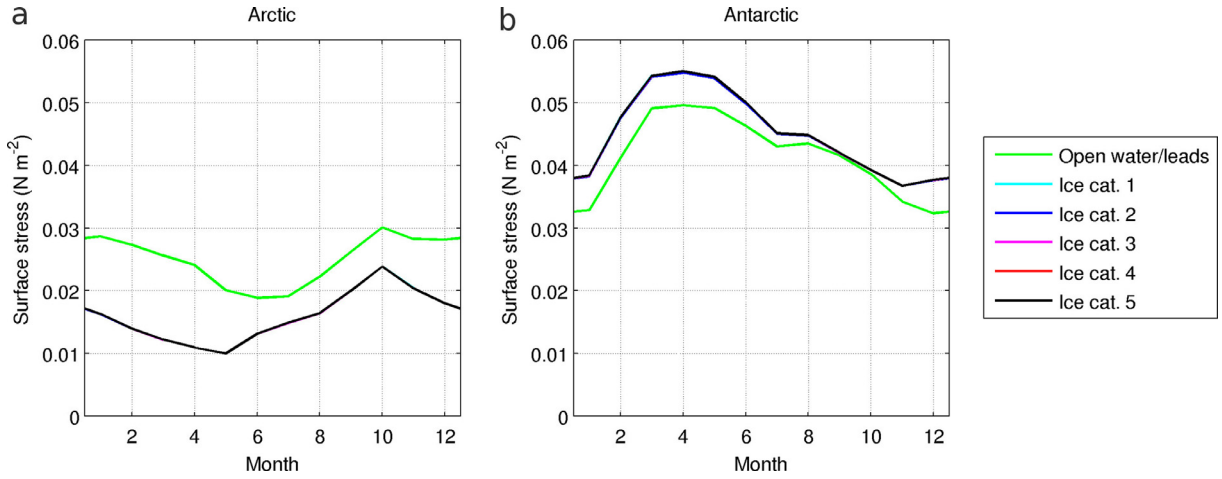

Fig. 10. Seasonal cycles of simulated surface stress norms in open water/leads and under ice, averaged in the areas depicted in Fig. 1 and where sea ice concentration exceeds 15%, in the Arctic (a) and the Antarctic (b). The seasonal cycles are identical for all ice categories.

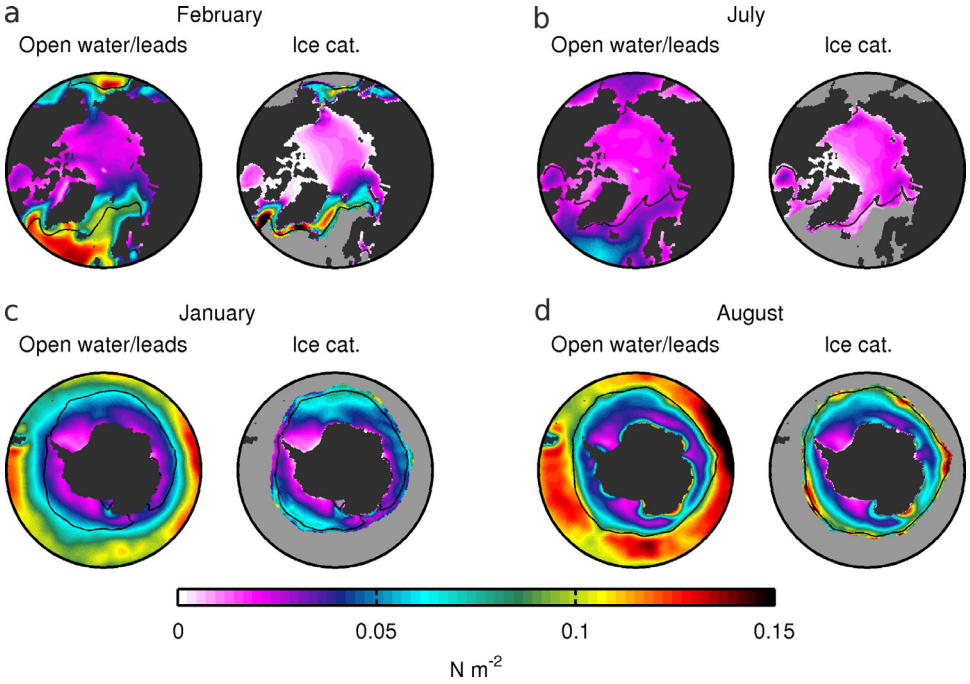

Fig. 11. Simulated surface stress norms in open water/leads and under ice, for February (a) and July (b) in the Arctic and for January (c) and August (d) in the Antarctic. The black lines correspond to the 15% ice concentration contours.

again point towards a lower heat supply from the subsurface in that hemisphere.

4.3. Surface stresses

Simulated surface stress norms are shown in Figs. 10 and 11. In open water, it actually corresponds to the wind stress. As parameterized in LIM, the ice-ocean stress is the same for all ice categories. Overall, surface stress is the SBC variable that differs the least between ice and open water in the model. Furthermore, it shows less seasonal variations than salt and heat fluxes. Maxima take place just after the sea ice extent minima, while minima occur a few months before. In the Arctic, stresses are typically 0.02 N m^{-2} in magnitude on average, and can be up to twice as large in the open water compared to the ice-covered fraction of grid cells. In the Antarctic, the typical norm of the surface stress is close to 0.045 N m^{-2}. It is slightly larger for ice than for open water and leads, which is made possible by the differences in drag coefficients between the atmosphere-ice and atmosphere-ocean interfaces (1.3×10^{-3} and 1×10^{-3}, respectively) and which reflects the more mobile nature of Antarctic sea ice compared to its Arctic counterpart.

In the Arctic, the spatial distribution of winter stresses in open water shows that surface winds are weak within the sea ice zone. Overall, stresses are small where ice concentrations are high, and larger where ice concentrations are low. Stresses are even smaller under ice, exceeding 0.05 N m^{-2} only in the Barents Sea, around Greenland and in the Bering Sea. Widespread areas of very low stresses along Siberia and in the CAA indicate almost motionless ice in the model. In July, winds appear to be weaker, mostly at lower latitudes, but the ice-ocean stresses start increasing in the inner pack as a result of a loosening and weakening sea ice cover.

Table 2
Integrated contributions of open water and leads (O.w./l.) and ice categories (1 to 5) to the total mean fluxes and stress seen by the ocean (Tot.), in the areas depicted in Fig. 1 and where sea ice concentration exceeds 15%. The winter (summer) month is February (July) in the Arctic and August (January) in the Antarctic. Mean fractions of open water/leads and ice categories are given (Frac.), along with corresponding contributions to salt (F_s), solar heat (F_{sol}) and non-solar heat (F_{nsol}) fluxes and to surface stress norms (τ).

	Frac. (%)		F_s (10^{-4} kg PSU m^{-2} s^{-1})		F_{sol} (W m^{-2})		F_{nsol} (W m^{-2})		τ (10^{-3} N m^{-2})	
	Win.	Sum.	Win.	Sum.	Win.	Sum.	Win.	Sum.	Win.	Sum.
Arctic										
O.w./l.	0.2	21.3	0.4	0.2	0.0	32.0	−0.3	−1.7	0.1	4.3
1	6.5	13.6	2.5	−15.7	0.0	3.7	−0.6	−7.4	1.9	2.4
2	32.3	22.0	5.2	−18.9	0.0	2.8	−1.3	−8.0	5.8	3.7
3	43.8	25.6	5.6	−13.2	0.0	1.2	−1.2	−5.7	4.7	3.6
4	9.6	8.9	0.8	−3.6	0.0	0.2	−0.3	−1.5	0.7	0.9
5	7.6	8.6	0.4	−3.7	0.0	0.0	−0.2	−2.4	0.7	1.0
Tot.	100.0	100.0	14.8	−54.8	0.0	39.8	−3.8	−26.7	14.0	15.8
Antarctic										
O.w./l.	0.4	28.3	1.1	−0.5	0.1	46.3	−0.8	−9.4	0.2	9.5
1	32.1	33.7	5.4	−20.7	0.0	0.6	−6.0	−13.9	16.9	14.1
2	61.1	31.7	2.1	−10.0	0.0	0.0	−8.5	−8.3	25.7	11.7
3	4.5	3.8	0.0	−0.9	0.0	0.0	−0.5	−0.9	1.4	1.0
4	0.4	0.5	−0.0	−0.2	0.0	0.0	−0.0	−0.2	0.1	0.1
5	1.5	2.0	0.4	−0.4	0.0	0.0	−0.2	−0.7	0.5	0.6
Tot.	100.0	100.0	9.1	−32.7	0.1	46.9	−16.0	−33.4	44.9	37.1

The Antarctic shares similarities with the NH, among which low winds and low open water stresses in summer and in regions of high ice concentrations. Differences include the presence of strong coastal winds in winter, resembling the katabatic winds existing in reality, which drive locally stresses up to 0.1 N m^{-2} in open water and are also visible in the under-ice fields. Much less ice is stationary along the coast than in the Arctic, reducing the regions where stresses are close to zero to small embayments barely visible in Fig. 11 and to the area close to the Amery Ice Shelf. The fact that Antarctic sea ice is thinner and not constrained in a basin implies that it is more tightly linked to winds, which is why the open water and ice stress maps match better than in the NH.

Our results are in line with Goosse and Fichefet (1999), who had already pointed out that the modifications of the stress at the ocean surface induced by the internal ice forces have only a regional effect.

4.4. Integrated contributions

Although a specific fraction of a grid cell may have the largest fluxes, its net contribution to sea surface changes depends on its area. Integrated contributions of open water and leads and ice categories to the total mean fluxes and stress seen by the ocean are thus given in Table 2 for the typical winter and summer months that we have considered so far. This gives an insight into their relative importance in the surface forcing of the ocean. With the exception of the solar heat flux, the results described hereafter show that the contribution of any ice category, even the thickest ones, can be dominant over open water because of a much higher concentration.

Although winter leads have the largest salt fluxes due to intense ice growth, they only contribute 3% to the total flux in the Arctic, and 12% in the Antarctic, due to their very small concentrations. Associating these fluxes to frazil ice formation in open water, these numbers suggest an model underestimation of the amount of ice produced in this way. In the Antarctic in particular, local observations indicate that possibly up to 50% of the ice volume originates from frazil (Wilchinsky et al., 2015, and references therein). In summer, the role of open water appears rather limited by weak freshwater fluxes, but this could be underestimated since lateral melt and runoff from ice are lacking in LIM. The salt budget is dominated in the NH by the first three categories, which combine non-negligible fluxes with high concentrations, and by the first two in the SH, mainly because they are the only ones with significant areas.

As suggested by previous results, almost all solar radiation reaches the ice-covered Southern Ocean through open water. Only 1% of the total energy is supplied through the first sea ice category. During July in the Arctic, the average solar heat flux amounts to nearly 40 W m^{-2}, among which 20% originates from radiation transmitted through the first three categories.

Since the non-solar heat flux and the surface stress are essentially the same for all ice classes, differences among them result from different mean areal coverage as well as distinct spatial distributions. Indeed, ice tends to be thinner in areas close to the edge where the oceanic heat flux is higher, which explains the large contribution of the first category relative to its mean concentration (particularly obvious in summer in the Antarctic). The non-solar heat loss in open water and leads is less than 10% of the total, except in January in the SH where it reaches 28%, mostly due to large open water fractions. The link between mean concentrations and integrated contributions is even stronger for the stress norm. This is consistent with a smaller spatial variability and with a lesser difference between the ice categories and the open water.

5. Conclusions

Sea ice being a fundamentally heterogeneous medium, its effects on the underlying ocean are highly spatially variable as well. Although most advanced sea ice models today attempt to represent the ice subgrid-scale heterogeneity by means of ice thickness distributions, the information about the spatial variability of surface boundary conditions is lost in the process of coupling them in a classic way to an ocean model. The present study is the first comprehensive examination of the simulated heterogeneity of ocean surface boundary conditions in an ocean-sea ice model including an ice thickness distribution, namely NEMO-LIM. The heterogeneous nature of atmosphere-ice interactions is a related and interesting question, that we have not addressed in this work.

The analysis of sea ice results in our simulation calls for two comments about ice thickness distributions in general. First, a recent study has shown that the commonly used number and boundaries of ice categories may not be optimal for an accurate representation of Arctic sea ice (Hunke, 2014). We have shown here that Antarctic sea ice is mostly confined in the two thinnest ice categories. Therefore, it is likely that in the current configuration we do not make the best use of the ice thickness distribution in the Southern Hemisphere. The second comment concerns the simulated concentrations of ice of given thickness ranges. A brief evaluation of NEMO-LIM results against IceBridge observations has indicated errors up to 50%, even when the mean modeled thickness is close to the observational estimate. A closer analysis of the origin of these errors, which could arise from biases in the large-scale sea ice deformation patterns or in the thickness redistribution process, is needed.

Our study has confirmed and quantified the high spatial variability of boundary conditions at the ocean surface in the sea ice zone in a model. Although large seasonal and geographical variations exist, the following conclusions can be drawn. The most striking contrast is between the open water/leads and ice-covered fractions of grid cells. Winter salt fluxes due to brine rejection during ice formation are up to an order of magnitude larger in leads than below ice. In summer, solar radiation can only penetrate the ocean through open water in the Antarctic. The situation is only slightly different in the Arctic, where some solar energy is transmitted through thin ice. Except in summer, the ocean cooling by non-solar heat fluxes is several times larger in the open water than under ice. Finally, the norm of the under-ice stress is up to 50% smaller than the wind stress in open water in the Arctic, whereas it is just a few percent larger in the Antarctic where sea ice is more mobile. This variable is nonetheless much less spatially variable than thermohaline fluxes. While the various sea ice categories are usually associated with smaller fluxes, integrated contributions (i.e. weighted by the concentrations) highlight their importance in the overall forcing of the ocean.

Even though they are of smaller magnitude than the ones between open water and ice-covered areas, significant differences also exist between the ice categories for the salt flux and for the solar heat flux in the Arctic. Since thin ice forms and melts faster, the simulated salt fluxes show a dependence on the ice thickness category in both hemispheres. In the Arctic, snow on top of the ice melts in summer, allowing solar radiation to be transmitted to the ocean. This results in different amounts of solar heat flux reaching the ice-ocean interface for different categories. In our model, the year-round presence of snow in most regions onto Antarctic sea ice prevents heterogeneities in transmitted shortwave radiation through the ice in the Southern Ocean.

The under-ice non-solar heat flux corresponds practically to the oceanic heat flux at the ice base. This flux is proportional to the difference between the sea surface temperature and the freezing point, which is determined by the sea surface salinity. Without a representation of the subgrid-scale heterogeneity of oceanic conditions under sea ice, the sea surface temperature and salinity are unique within one grid cell, and the oceanic heat flux is necessary identical for all thickness categories. On the other hand, the homogeneity of the ice-ocean stress results from the use in the model of a simple parameterization with a constant drag coefficient. More advanced formulations of the drag coefficient would introduce variability in the surface stress among the categories as well (e.g., Tsamados et al., 2014).

The present work is intended to serve as a guideline for the understanding of small-scale ice-ocean processes, and in particular for the implementation of subgrid-scale ocean vertical mixing schemes under sea ice. Such a scheme has been developed, tested and evaluated in a parallel study (Barthélemy et al., 2016), which revisits and generalizes the work of Holland (2003) and Jin et al. (2015). The main principle is to replicate, at each grid point, the mixed layer computations in sub-columns corresponding to open water and to the ice thickness categories. Thus, this method makes use of the subgrid-scale surface boundary condition variables, instead of leaving them as mere diagnostics. It allows to represent specific oceanic conditions in open water and under each category.

One of the main results of this follow-up study is that heterogeneities in surface boundary conditions are associated in winter with a pronounced subgrid-scale variability in the depth of convective mixing. At low temperatures, the surface buoyancy fluxes are indeed tightly linked to salt fluxes. In certain conditions, the most intense brine rejections occurring in leads are able to generate convection reaching depths greater than the mixed layer, hence affecting the heat and salt budgets of the latter. In summer, the subgrid-scale distribution of the solar heat flux has clear consequences. Open waters within the sea ice zone become significantly warmer than the freezing point. Performing fully coupled simulations, in which this warming could trigger important feedback processes, would be a useful further step. Besides, the differential heating of the under-ice waters leads to an oceanic heat flux at the ice base that is larger for thinner ice. Faster melt of thin ice could thereby enhance the ice-albedo feedback (e.g., Maykut and Perovich, 1987). Finally, as demonstrated by Long et al. (2015), representing the subgrid-scale heterogeneity of shortwave radiation is also required to simulate correctly the primary productivity in sea ice-covered waters.

Acknowledgements

A. Barthélemy and H. Goosse are respectively Research Assistant and Research Director with the Fonds de la Recherche Scientifique (F.R.S.-FNRS/Belgium), which supports this work. Computational resources have been provided by the supercomputing facilities of the Université catholique de Louvain (CISM/UCL) and the Consortium des Equipements de Calcul Intensif en Fédération Wallonie Bruxelles (CECI) funded by the F.R.S.-FNRS under convention 2.5020.11. We are grateful to Gurvan Madec, Martin Vancoppenolle, Julien Le Sommer and Eric Deleersnijder for their careful reading of the original manuscript. We also thank two anonymous reviewers for their valuable comments that contributed to improve this manuscript.

Supplementary material

Supplementary material associated with this article can be found, in the online version, at 10.1016/j.ocemod.2016.05.003

References

Arndt, S., Nicolaus, M., 2014. Seasonal cycle and long-term trend of solar energy fluxes through arctic sea ice. Cryosphere 8, 2219–2233. doi:10.5194/tc-8-2219-2014.

Barthélemy, A., Fichefet, T., Goosse, H., Madec, G., 2015. Modeling the interplay between sea ice formation and the oceanic mixed layer: Limitations of simple brine rejection parameterizations. Ocean Modell. 86, 141–152. doi:10.1016/j.ocemod.2014.12.009.

Barthélemy, A., Fichefet, T., Goosse, H., Madec, G., 2016. A multi-column vertical mixing scheme to parameterize the heterogeneity of oceanic conditions under sea ice. Ocean Modell., 2016, under review.

Barthélemy, A., Goosse, H., Mathiot, P., Fichefet, T., 2012. Inclusion of a katabatic wind correction in a coarse-resolution global coupled climate model. Ocean Modell. 48, 45–54. doi:10.1016/j.ocemod.2012.03.002.

Behrendt, A., Dierking, W., Witte, H., 2015. Thermodynamic sea ice growth in the central weddell sea, observed in upward-looking sonar data. J. Geophys. Res. Oceans 120, 2270–2286. doi:10.1002/2014JC010408.

Berliand, M.E., Strokina, T.G., 1980. Global distribution of the total amount of clouds (in Russian). Technical report. Hydrometeorological Publishing House, Leningrad, Russia.

Blanke, B., Delecluse, P., 1993. Variability of the tropical atlantic ocean simulated by a general circulation model with two different mixed-layer physics. J. Phys. Oceanogr. 23, 1363–1388. doi:10.1175/1520-0485(1993)023⟨1363:VOTTAO⟩2.0.CO;2.

Bouillon, S., Fichefet, T., Legat, V., Madec, G., 2013. The elastic-viscous-plastic method revisited. Ocean Modell. 71, 2–12. doi:10.1016/j.ocemod.2013.05.013.

Castro-Morales, K., Kauker, F., Losch, M., Hendricks, S., Riemann-Campe, K., Gerdes, R., 2014. Sensitivity of simulated arctic sea ice to realistic ice thickness distributions and snow parameterizations. J. Geophys. Res. Oceans 119, 559–571. doi:10.1002/2013JC009342.

Cavalieri, D.J., Parkinson, C.L., Gloersen, P., Zwally, H., 1996. Sea ice xoncentrations from Nimbus-7 SMMR and DMSP SSM/I-SSMIS passive microwave data. NASA National Snow and Ice Data Center Distributed Active Archive Center, Boulder, Colorado, USA doi:10.5067/8GQ8LZQVL0VL. [1979–2010]

Comiso, J.C., 2000. Bootstrap sea ice concentrations from Nimbus-7 SMMR and DMSP SSM/I-SSMIS. NASA National Snow and Ice Data Center Distributed Active Archive Center, Boulder, Colorado, USA doi:10.5067/J6JQLS9EJ5HU. Version 2 [1979–2012]

Conkright, M.E., Locarnini, R.A., Garcia, H.E., O'Brien, T.D., Boyer, T.P., Stephens, C., Antonov, J.I., 2002. World Ocean Atlas 2001. National Oceanographic Data Center, Silver Spring, Maryland, USA Digital media.

Curry, J.A., Schramm, J.L., Ebert, E.E., 1995. Sea ice-albedo climate feedback mechanism. J. Climate 8, 240–247. doi:10.1175/1520-0442(1995)008⟨0240:SIACFM⟩2.0.CO;2.

Dai, A., Trenberth, K.E., 2002. Estimates of freshwater discharge from continents: Latitudinal and seasonal variations. J. Hydrometeor. 3, 660–687. doi:10.1175/1525-7541(2002)003⟨0660:EOFDFC⟩2.0.CO;2.

Duffy, P.B., Caldeira, K., 1997. Sensitivity of simulated salinity in a three-dimensional ocean model to upper ocean transport of salt from sea-ice formation. Geophys. Res. Lett. 24, 1323–1326. doi:10.1029/97GL01294.

Goosse, H., 1997. Modelling the large-scale behaviour of the coupled ocean-sea-ice system. Université catholique de Louvain Ph.D. thesis.

Goosse, H., Fichefet, T., 1999. Importance of ice-ocean interactions for the global ocean circulation: A model study. J. Geophys. Res. 104, 23337–23355. doi:10.1029/1999JC900215.

Haid, V., Timmermann, R., 2013. Simulated heat flux and sea ice production at coastal polynyas in the southwestern weddell sea. J. Geophys. Res. Oceans 118, 2640–2652. doi:10.1002/jgrc.20133.

Hibler, W.D., 1980. Modeling a variable thickness sea ice cover. Mon. Wea. Rev. 108, 1943–1973. doi:10.1175/1520-0493(1980)108⟨1943:MAVTSI⟩2.0.CO;2.

Holland, M.M., 2003. An improved single-column model representation of ocean mixing associated with summertime leads: Results from a SHEBA case study. J. Geophys. Res. 108, 3107. doi:10.1029/2002JC001557.

Hudson, S.R., Granskog, M.A., Sundfjord, A., Randelhoff, A., Renner, A.H.H., Divine, D.V., 2013. Energy budget of first-year arctic sea ice in advanced stages of melt. Geophys. Res. Lett. 40, 2679–2683. doi:10.1002/grl.50517.

Hunke, E.C., 2014. Sea ice volume and age: Sensitivity to physical parameterizations and thickness resolution in the CICE sea ice model. Ocean Modell. 82, 45–59. doi:10.1016/j.ocemod.2014.08.001.

Hunke, E.C., Lipscomb, W.H., Turner, A.K., Jeffery, N., Elliott, S., 2015. CICE: the Los Alamos Sea Ice Model Documentation and Software User's Manual. Technical report la-cc-06-012. Los Alamos National Laboratory, Los Alamos, New Mexico. Version 5.1

Jin, M., Hutchings, J., Kawaguchi, Y., 2015. Sensitivity study of subgrid scale ocean mixing under sea ice using a two-column ocean grid in climate model CESM. Front. Earth Sci. 9, 594–604. doi:10.1007/s11707-014-0489-9.

Kalnay, E., Kanamitsu, M., Kistler, R., Collins, W., Deaven, D., Gandin, L., Iredell, M., Saha, S., White, G., Woollen, J., Zhu, Y., Leetmaa, A., Reynolds, R., Chelliah, M., Ebisuzaki, W., Higgins, W., Janowiak, J., Mo, K.C., Ropelewski, C., Wang, J., Jenne, R., Joseph, D., 1996. The NCEP/NCAR 40-year reanalysis project. Bull. Amer. Meteor. Soc. 77, 437–471. doi:10.1175/1520-0477(1996)077⟨0437:TNYRP⟩2.0.CO;2.

Komuro, Y., 2014. The impact of surface mixing on the arctic river water distribution and stratification in a global ice-ocean model. J. Climate 27, 4359–4370. doi:10.1175/JCLI-D-13-00090.1.

Komuro, Y., Suzuki, T., 2013. Impact of subgrid-scale ice thickness distribution on heat flux on and through sea ice. Ocean Modell. 71, 13–25. doi:10.1016/j.ocemod.2012.08.004.

Krishfield, R.A., Perovich, D.K., 2005. Spatial and temporal variability of oceanic heat flux to the arctic ice pack. J. Geophys. Res. 110, C07021. doi:10.1029/2004JC002293.

Kurtz, N., Studinger, M.S., Harbeck, J., Onana, V., Farrell, S., 2012. NASA National Snow and Ice Data Center Distributed Active Archive Center, Boulder, Colorado, USA doi:10.5067/7XJ9HRV50O57. [2009–2010]

Kurtz, N., Studinger, M.S., Harbeck, J., Onana, V., Yi, D., 2015. NASA National Snow and Ice Data Center Distributed Active Archive Center, Boulder, Colorado, USA doi:10.5067/G519SHCKWQV6. [2009–2013]

Kurtz, N.T., Farrell, S.L., Studinger, M., Galin, N., Harbeck, J.P., Lindsay, R., Onana, V.D., Panzer, B., Sonntag, J.G., 2013. Sea ice thickness, freeboard, and snow depth products from operation icebridge airborne data. Cryosphere 7, 1035–1056. doi:10.5194/tc-7-1035-2013.

Large, W.G., Yeager, S.G., 2004. Diurnal to decadal global forcing for ocean and sea-ice models: The data sets and flux climatologies. Technical report. National Center for Atmospheric Research, Boulder, Colorado, USA.

Lecomte, O., Fichefet, T., Flocco, D., Schroeder, D., Vancoppenolle, M., 2015. Interactions between wind-blown snow redistribution and melt ponds in a coupled ocean-sea ice model. Ocean Modell. 87, 67–80. doi:10.1016/j.ocemod.2014.12.003.

Lecomte, O., Fichefet, T., Vancoppenolle, M., Domine, F., Massonnet, F., Mathiot, P., Morin, S., Barriat, P., 2013. On the formulation of snow thermal conductivity in large-scale sea ice models. J. Adv. Model. Earth Syst. 5, 542–557. doi:10.1002/jame.20039.

Long, M.C., Lindsay, K., Holland, M.M., 2015. Modeling photosynthesis in sea ice-covered waters. J. Adv. Model. Earth Syst. 7, 1189–1206. doi:10.1002/2015MS000436.

Losch, M., Herlufsen, S., Timmermann, R., 2006. Effects of heterogeneous surface boundary conditions on parameterized oceanic deep convection. Ocean Modell. 13, 156–165. doi:10.1016/j.ocemod.2005.12.003.

Madec, G., 2008. NEMO ocean engine. Note du Pôle de modélisation, 27. Institut Pierre-Simon Laplace, France. ISSN No 1288-1619

Madec, G., Imbard, M., 1996. A global ocean mesh to overcome the north pole singularity. Clim. Dynam. 12, 381–388. doi:10.1007/BF00211684.

Massonnet, F., Fichefet, T., Goosse, H., Vancoppenolle, M., Mathiot, P., König Beatty, C., 2011. On the influence of model physics on simulations of arctic and antarctic sea ice. Cryosphere 5, 687–699. doi:10.5194/tc-5-687-2011.

Massonnet, F., Mathiot, P., Fichefet, T., Goosse, H., König Beatty, C., Vancoppenolle, M., Lavergne, T., 2013. A model reconstruction of the antarctic sea ice thickness and volume changes over 1980-2008 using data assimilation. Ocean Modell. 64, 67–75. doi:10.1016/j.ocemod.2013.01.003.

Maykut, G.A., McPhee, M.G., 1995. Solar heating of the arctic mixed layer. J. Geophys. Res. 100, 24691–24703. doi:10.1029/95JC02554.

Maykut, G.A., Perovich, D.K., 1987. The role of shortwave radiation in the summer decay of a sea ice cover. J. Geophys. Res. 92, 7032–7044. doi:10.1029/JC092iC07p07032.

McPhee, M.G., 1992. Turbulent heat flux in the upper ocean under sea ice. J. Geophys. Res. 97, 5365–5379. doi:10.1029/92JC00239.

McPhee, M.G., Kikuchi, T., Morison, J.H., Stanton, T.P., 2003. Ocean-to-ice heat flux at the north pole environmental observatory. Geophys. Res. Lett. 30, 2274. doi:10.1029/2003GL018580.

McPhee, M.G., Kottmeier, C., Morison, J.H., 1999. Ocean heat flux in the central weddell sea during winter. J. Phys. Oceanogr. 29, 1166–1179. doi:10.1175/1520-0485(1999)029⟨1166:OHFITC⟩2.0.CO;2.

Nguyen, A.T., Menemenlis, D., Kwok, R., 2009. Improved modeling of the arctic halocline with a subgrid-scale brine rejection parameterization. J. Geophys. Res. 114, C11014. doi:10.1029/2008JC005121.

Nicolaus, M., Katlein, C., Maslanik, J., Hendricks, S., 2012. Changes in arctic sea ice result in increasing light transmittance and absorption. Geophys. Res. Lett. 39, L24501. doi:10.1029/2012GL053738.

Nihashi, S., Ohshima, K.I., 2015. Circumpolar mapping of antarctic coastal polynyas and landfast sea ice: Relationship and variability. J. Climate 28, 3650–3670. doi:10.1175/JCLI-D-14-00369.1.

Perovich, D.K., Elder, B., 2002. Estimates of ocean heat flux at SHEBA. Geophys. Res. Lett. 29, 1344. doi:10.1029/2001GL014171.

Pringle, D.J., Eicken, H., Trodahl, H.J., Backstrom, L.G.E., 2007. Thermal conductivity of landfast antarctic and arctic sea ice. J. Geophys. Res. 112, C04017. doi:10.1029/2006JC003641.

Roullet, G., Madec, G., 2000. Salt conservation, free surface, and varying levels: A new formulation for ocean general circulation models. J. Geophys. Res. 105, 23927–23942. doi:10.1029/2000JC900089.

Rousset, C., Vancoppenolle, M., Madec, G., Fichefet, T., Flavoni, S., Barthélemy, A., Benshila, R., Chanut, J., Levy, C., Masson, S., Vivier, F., 2015. The louvain-la-neuve sea ice model LIM3.6: global and regional capabilities. Geosci. Model Dev. 8, 2991–3005. doi:10.5194/gmd-8-2991-2015.

Schmidt, G.A., Bitz, C.M., Mikolajewicz, U., Tremblay, L.B., 2004. Ice-ocean boundary conditions for coupled models. Ocean Modell. 7, 59–74. doi:10.1016/S1463-5003(03)00030-1.

Schweiger, A., Lindsay, R., Zhang, J., Steele, M., Stern, H., Kwok, R., 2011. Uncertainty in modeled arctic sea ice volume. J. Geophys. Res. 116, C00D06. doi:10.1029/2011JC007084.

Sirevaag, A., McPhee, M.G., Morison, J.H., Shaw, W.J., Stanton, T.P., 2010. Wintertime mixed layer measurements at maud rise, weddell sea. J. Geophys. Res. 115, C02009. doi:10.1029/2008JC005141.

Stanton, T.P., Shaw, W.J., Hutchings, J.K., 2012. Observational study of relationships between incoming radiation, open water fraction, and ocean-to-ice heat flux in the transpolar drift: 2002-2010. J. Geophys. Res. 117, n/a–n/a. doi:10.1029/2011JC007871.

Steele, M., Morley, R., Ermold, W., 2001. PHC: A global ocean hydrography with a high-quality arctic ocean. J. Climate 14, 2079–2087. doi:10.1175/1520-0442(2001)014⟨2079:PAGOHW⟩2.0.CO;2.

Thorndike, A.S., Rothrock, D.A., Maykut, G.A., Colony, R., 1975. The thickness distribution of sea ice. J. Geophys. Res. 80, 4501–4513. doi:10.1029/JC080i033p04501.

Trenberth, K.E., Large, W.G., Olson, J.G., 1989. Global Ocean Wind Stress, climatology and monthly, by Trenberth et al. National Center for Atmospheric Research, Boulder, Colorado, USA Digital media.

Tsamados, M., Feltham, D.L., Schroeder, D., Flocco, D., Farrell, S.L., Kurtz, N., Laxon, S.W., Bacon, S., 2014. Impact of variable atmospheric and oceanic form drag on simulations of arctic sea ice. J. Phys. Oceanogr. 44, 1329–1353. doi:10.1175/JPO-D-13-0215.1.

Vancoppenolle, M., Fichefet, T., Goosse, H., Bouillon, S., Madec, G., Morales Maqueda, M.A., 2009. Simulating the mass balance and salinity of arctic and antarctic sea ice. 1. model description and validation. Ocean Modell. 27, 33–53. doi:10.1016/j.ocemod.2008.10.005.

Vancoppenolle, M., Meiners, K.M., Michel, C., Bopp, L., Brabant, F., Carnat, G., Delille, B., Lannuzel, D., Madec, G., Moreau, S., Tison, J.L., van der Merwe, P., 2013. Role of sea ice in global biogeochemical cycles: emerging views and challenges. Quaternary Sci. Rev. 79, 207–230. doi:10.1016/j.quascirev.2013.04.011.

Wilchinsky, A.V., Heorton, H.D.B.S., Feltham, D.L., Holland, P.R., 2015. Study of the impact of ice formation in leads upon the sea ice pack mass balance using a new frazil and grease ice parameterization. J. Phys. Oceanogr. 45, 2025–2047. doi:10.1175/JPO-D-14-0184.1.

Worby, A.P., Geiger, C.A., Paget, M.J., Van Woert, M.L., Ackley, S.F., DeLiberty, T.L., 2008. Thickness distribution of antarctic sea ice. J. Geophys. Res. 113, C05S92. doi:10.1029/2007JC004254.

Zhang, J., Rothrock, D.A., 2003. Modeling global sea ice with a thickness and enthalpy distribution model in generalized curvilinear coordinates. Mon. Wea. Rev. 131, 845–861. doi:10.1175/1520-0493(2003)131⟨0845:MGSIWA⟩2.0.CO;2.

Zhang, J., Steele, M., 2007. Effect of vertical mixing on the atlantic water layer circulation in the arctic ocean. J. Geophys. Res. 112, C04S04. doi:10.1029/2006JC003732.